Columnar Liquid Crystals in Cylindrical Nanoconfinement

Ruibin Zhang,[†] Xiangbing Zeng,[†] Bongseock Kim,[‡] Richard J. Bushby,[§] Kyusoon Shin,[∥] Patrick J. Baker,[⊥] Virgil Percec,[#] Pawaret Leowanawat,[#] and Goran Ungar*[,⊗,†]

[†]Department of Materials Science and Engineering, University of Sheffield, Sheffield S1 3JD, U.K., [‡]School of Chemical and Biological Engineering, Seoul National University, 151-742 Seoul, Republic of Korea, [§]School of Chemistry, University of Leeds, Leeds LS2 9JT, U.K., [∥]Advanced Institute of Research, Dongjin Semichem Company, Seongnam, Gyeonggi-do 463-400, Republic of Korea, [⊥]Department of Molecular Biology and Biotechnology, University of Sheffield, Sheffield S10 2TN, U.K., [#]Roy & Diana Vagelos Laboratories, Department of Chemistry, University of Pennsylvania, Philadelphia, Pennsylvania 19104-6323, United States, and [⊗]Department of Physics, Zhejiang Sci-Tech University, Xiasha College Park, 310018 Hangzhou, China

ABSTRACT Axial orientation of discotic columnar liquid crystals in nanopores of inorganic templates, with the columns parallel to the axis of the nanochannels, is considered desirable for applications such as production of molecular wires. Here, we evaluate experimentally the role of the rigidity of the LC columns in achieving such orientation in nanopores where the planar anchoring (*i.e.*, columns parallel to wall surface) is enforced. We studied the columnar phase of several discotic compounds with increasing column rigidity in the following order: dendronized carbazole, hexakis(hexyloxy)triphenylene (HAT6), a 1:1 HAT6-trinitrofluorenone (TNF) complex, and a helicene derivative. Using 2-D X-ray diffraction, AFM, grazing incidence diffraction, and polarized microscopy, we observed that the orientation of the columns changes from circular concentric to axial with increasing column rigidity. Additionally, when the rigidity is borderline, increasing pore diameter can change the configuration from axial back to circular. We derive expressions for distortion free energy that suggest that the orientation is determined by the competition between, on the one hand, the distortion energy of the 2-d lattice and the mismatch of its crystallographic facets with the curved pore wall in the axial orientation and, on the other hand, the bend energy of the columns in the circular configuration. Furthermore, the highly detailed AFM images of the core of the disclinations of strength +1 and +1/2 in the center of the pore reveal that the columns spiral down to the very center of the disclination and that there is no amorphous or misaligned region at the core, as suggested previously.

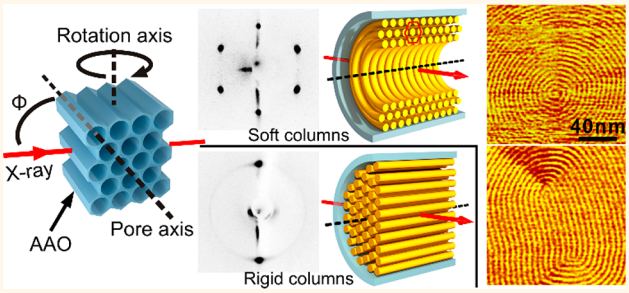

KEYWORDS: columnar liquid crystals · discotics · confinement · anodic aluminum oxide · nanopores · orientation · rigidity · AFM · X-ray diffraction · SAXS · GISAXS · disclinations

Due to $\pi-\pi$ stacking of neighboring aromatic cores, discotic columnar liquid crystals (DCLC) can form charge carrier pathways along the columnar direction and therefore behave as organic semiconductors.[1−4] Confining DCLC in linear nanopores within inorganic templates and subsequently dissolving the template is a promising way of fabricating organic nanowires, directed light-emitting diodes, *etc*. Furthermore, a nanoporous anodized alumina (AAO) layer can improve light extraction efficiency of LEDs.[5] However, the key prerequisite for the successful application of this technique is the ability to control column orientation in the nanopores. For example, an axial orientation, where the columns are parallel to the long axis of the pores, is desirable for fabricating organic electronic devices. The studies performed so far have suggested that axial orientation of columns is hard to achieve.[6,7] A mixture of axial and radial orientation has been reported for discotics of small cores,[8,9] and a pure axial orientation has been reported only for a large core discotic.[10,11]

The configuration of the columnar phase in nanopores is strongly affected by the mode of molecular anchoring on the surface of the inner wall. Axial orientation is expected to be more likely if the columns prefer to lie parallel to the pore surface (planar anchoring) rather than perpendicular to it (homeotropic anchoring). In the case of axial orientation, the columns would experience no bend, splay, or twist deformation (see Figure S5 in the Supporting Information). It may therefore seem

* Address correspondence to g.ungar@sheffield.ac.uk.

Received for review November 19, 2014 and accepted January 27, 2015.

Published online January 27, 2015
10.1021/nn506605p

surprising that axial orientation is rarely obtained. The alternative seems to be more common, even though it involves bend deformation. We have observed previously that liquid crystal (LC) columns consisting of T-shaped amphiphilic molecules adopt the concentric circular (CC) configuration and can tolerate very high curvature.[7] Monte Carlo simulations predict both orientations for discotics under different conditions.[12] The situation may be compared to that in confined nematic LCs,[13,14] although, as will be shown, there are significant differences. In the present systematic investigation of the configuration of nanoconfined columnar LCs we show that by increasing the rigidity of the columns and reducing the pore diameter the axial orientation can become favorable, and we develop an energy argument for its rare occurrence. At the soft end we use taper-shaped "minidendrons" forming self-assembled discs; for medium stiff columns, we use a classic discotic triphenylene derivative as well as its more rigid complex. At the rigid end we choose a helicene discotic LC derivative forming stiff six-stranded helical columns. Column configuration is determined by a combination of X-ray reciprocal space mapping, grazing incidence small-angle X-ray scattering (GISAXS) and atomic force microscopy (AFM). For clarity, here we concentrate only on cases of planar anchoring, where the columns prefer to align parallel to the substrate surface.

Figure 1 summarizes the compounds used in this study. The compound referred to as "CBZ dendron" is a dendronized electron-donating carbazole (Figure 1a).[15] It self-assembles into columns of the hexagonal columnar phase (Col_{hex}), consisting of π-stacked donors in the center and semiperfluorinated alkyl tails at the periphery of the columns. The small core discotic is 2,3,6,7,10,11-hexakis(hexyloxy)triphenylene (HAT6) (Figure 1b). HAT6 was also doped with 2,4,7-trinitro-9-fluorenone (TNF) in a 1:1 molar ratio to produce the more rigid TNF columnar complex.[16,17] The helicene studied here is a racemic tetraalkoxy derivative of a heterohelicene synthesized by the Katz group at Columbia University.[18] The columns it forms are hollow 13_2 helices with each asymmetric unit comprising six molecules; hence, the columns are rigid six-stranded helices (Figure 1c).[19]

The ranking in order of increasing bend elastic constants K_3 should be CBZ dendron, HAT6, HAT6-TNF complex, helicene. The fraction of main (non-H, non-F) atoms in the stiff aromatic portion of the molecule is around 30% for the CBZ dendron and HAT6 and about 40% in the HAT6—TNF complex and the helicene. Furthermore, bending of columns involves increasing the average distance between the aromatic discs, the more so the larger the disc. Thus, the increased charge transfer interaction is likely to additionally enhance the stiffness of the HAT6-TNF complex relative to that of pure HAT. Similarly, the

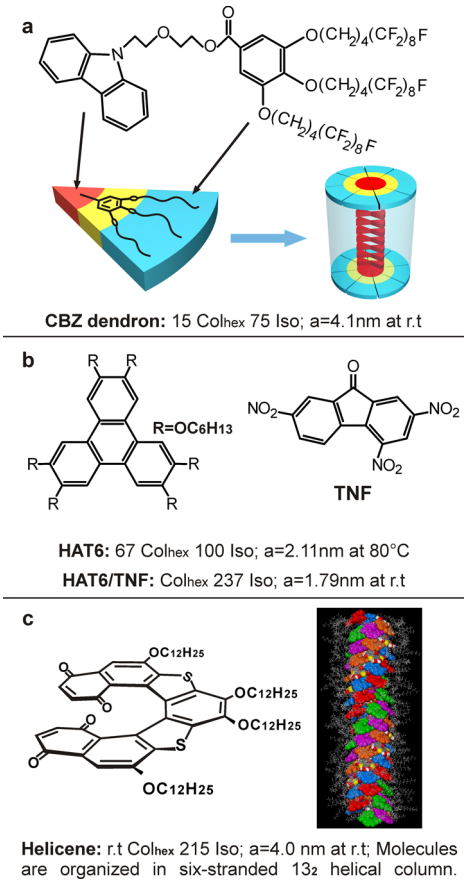

Figure 1. Structures of the compounds studied,[15−19] their phase types, transition temperatures (°C), and lattice parameters as bulk materials.

large disc size and the large diameter of the interwoven multiple stranded cores are both likely to add to the stiffness of helicene columns. Finally, the high isotropization temperatures T_i of the complex and the helicene compared to those of the dendron and HAT6 (Figure 1) support our ranking as $T_i = \Delta H_i/\Delta S_i$; both the increasing π-interaction (increasing transition enthalpy ΔH_i) and increasing stiffness (decreasing entropy ΔS_i) are reflected in the high T_i of the complex and the helicene.

RESULTS AND DISCUSSION

1. CBZ Dendron. The bulk material forms the Col_{hex} phase between 15 and 75 °C. When cooled from the isotropic to room temperature (rt) at 0.1 °C/min the columns adopt planar orientation relative to the glass surface, as evidenced by the birefringent texture of the dendron sandwiched between two glass slides (Supporting Information, Figure S1a). The geometry of the 2d X-ray diffraction experiment is shown in Figure 2a. The template membrane was mounted vertically on a motorized goniometer that can rotate about the vertical axis. The rotation angle Φ is the angle between the incident X-ray beam and the AAO pore axis. $\Phi = 0$ when the incident beam is parallel to

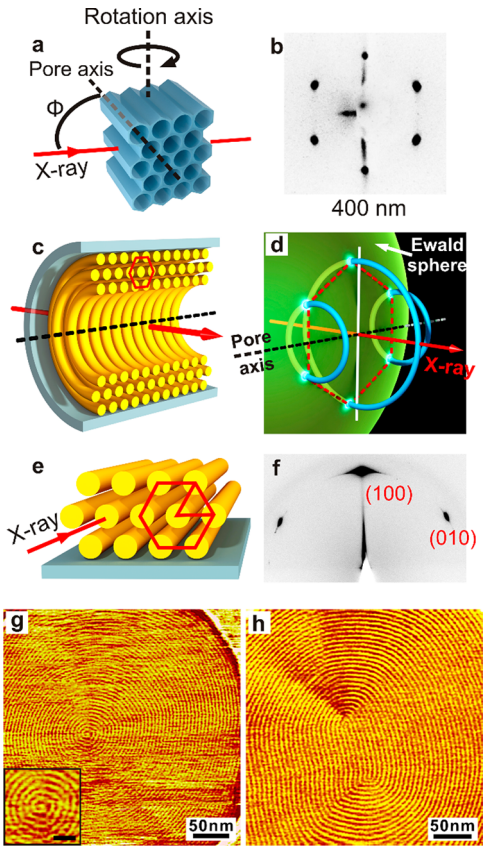

Figure 2. (a) Geometry of the X-ray diffraction setup. The rotation angle Φ is the angle between the incident beam and the AAO pore axis. (b) SAXS patterns of CBZ dendron in 400 nm template, recorded at Φ = 80°. (c, d) Circular concentric configuration of LC columns inside the pore (schematic) and the corresponding cylindrically averaged reciprocal space, showing the three {100} rings cutting the Ewald sphere of reflection at Φ = 80° (compare their six intersections with the Ewald sphere with the six diffraction spots in (b)). (e) Model of the alignment of the Col_{hex} phase on a flat substrate with the {100} plane parallel to the surface, based on the GISAXS pattern (f) obtained from CBZ dendron on a horizontally mounted silica substrate. (g, h) AFM phase images of CBZ dendron in 400 nm pores of circular and slightly elliptical cross-section, respectively (bright = harder aromatic core, dark = softer semifluorinated alkyl chains; bar in inset = 8 nm).

the pore axis. The largest practical Φ in our experiments is ca. 80°, as absorption would prevent recording at Φ = 90°. At Φ = 80°, the AAO template with 400 nm pore diameter filled with CBZ dendron shows a hexagonal pattern of {100} diffraction spots (Figure 2b). Patterns recorded at other Φ angles are shown in Figure S2 (Supporting Information). The lattice spacing d_{10} = 3.9 nm is the same as that measured on the bulk sample in the Col_{hex} phase.[15] The six-spot diffraction pattern indicates that the columns are perpendicular to the pore axis. The 20 and 70 nm template samples also show similar diffraction patterns except for the increased diffraction spot broadening associated with reduced coherently diffracting domain size (Figure S3, Supporting Information)).

The 3-d reciprocal space in the region of the {100} reflection group cutting the Ewald sphere at Φ = 80° is schematically drawn in Figure 2d. Under planar anchoring condition, a CC configuration is a possible option (Figure 2c). That this is indeed the actual case is proven by AFM observation: the AFM phase image obtained from the top of a circular 400 nm pore clearly shows that individual columns run parallel to the wall and form circles (Figure 2g,h). Interestingly, in strictly circular pores (Figure 2g), the columns form a disclination of strength +1 in the center of the pore. The detail revealed by the AFM image shows that, in fact, on the molecular scale, a plane normal to the pore axis contains just one spiralling column, rather than a series of circular columns of ever decreasing diameter. In contrast, in the pores that are slightly elliptical (Figure 2h), the columns form two separate $S = +1/2$ disclinations. This time, the pore cross-section plane contains two intertwined spiralling columns, each ending at one of the two 1/2-strength disclinations. In fact, in the case of the slightly elliptical pore (Figure 2h) the spirals are distorted, particularly near the center of the pore, consisting of parallel straight and curved sections ("racetrack geometry"). This geometry minimizes the energetically prohibitive splay deformation that would be required if circular columns in the center of the pore were to match elliptical columns at the periphery. These observations are consistent with our previous conclusion that the configuration of columns at the center is strongly affected by small distortions of the pore wall.[7]

It is interesting to compare the above behavior of columnar LCs with that of the discotic nematic (N_D) phase in extruded fibers of carbonaceous pitches, the precursors of carbon fibers.[20−22] The theory of these[23] shows that whether one ends up with a single $S = 1$ disclination or a pair of $S = 1/2$ disclinations depends not on the shape of the boundary (round or oval), since there the shape is self-adjusting, but on the balance of the bend and splay terms. The key difference between the cases of N_D and Col_{hex} phases here is the very much higher splay term in the latter case.[24]

The images in Figure 2g,h represent "pinned" developable domains.[25−27] This means that the columns lie on developable surfaces, in this case scrolls, *i.e.*, surfaces having the centers of curvature on a straight line, the line in this case being parallel to the pore axis. It is particularly interesting to note that in Figure 2g,h, toward the center of these structures, the curvature approaches the intercolumn separation, something that previous workers have doubted to be possible![27] Previously, it has been speculated that the columns may be describing involutes of a central cylindrical region of an $S = 1$ disclination of radius r_c (see Figure 5b).[26,28] As to the nature of the central region, it has been further speculated that this may be filled with isotropic liquid or a bundle of hexagonal axial columns

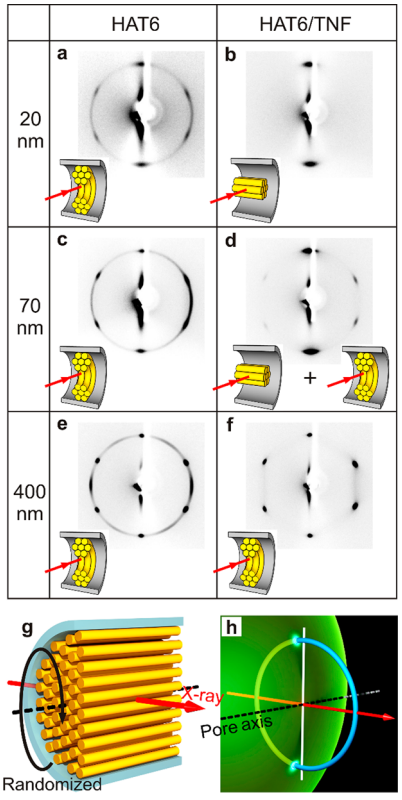

Figure 3. SAXS patterns of HAT6 (a, c, e) and HAT6-TNF complex (b, d, f) in HTS-treated AAO templates recorded at $\Phi = 80°$. The added icons show the column arrangement in the nanopores and the direction of the X-ray beam. (g) Schematic of discotic columns oriented axially in the pore, with the circular arrow indicating random orientation of the lattice in different pores with a common *z*-axis along the pore axis. (h) Sketch of the reciprocal space equivalent to the real space in (g), cut by the Ewald sphere and giving rise to the two equatorial reflections.

(see Figure 5c).[26−29] As we can see from Figure 2g, at least in the flexible columns of the CBZ dendron, such a central region does not exist. Similarly, recent detailed AFM images of small circular droplets of another column-forming compound have shown concentric circular columns to come right down to the center of the disclination, as in Figure 5a, again without a distinct central region.[7] In contrast, in another discotic triphenylene derivative, based on measurements of compressibility and bend modulus, the estimate of r_c gave a value of 35 nm[29] or even significantly larger if some other reported values of elastic constants were used. Notwithstanding our AFM observations reported here, we do not exclude the possibility that a distinct central core may exist in the case of stiffer columns that we could not image due to their small diameter. In fact there is some indication from X-ray diffraction that an axial core may exist in the HAT6-TNF complex (Figure 3d), although the evidence is weak. A similar core−shell arrangement has also been proposed in ref 8. Finally, we note that in no case have we observed an instance of "escape in the third dimension", often found in the center of $S = 1$ disclinations in nematic LCs.

Another interesting feature we observed is the fact that a {100} plane of the hexagonal lattice invariably lies parallel to the pore axis, hence a [100] crystallographic direction is perpendicular to the pore wall and a [110] direction is parallel to the pore axis. Indeed, GISAXS on a thin film of the dendron on a flat silicon substrate shows a strong preference for a {100} plane to lie parallel to the substrate (Figure 2e,f).[30] This is consistent with the just described preferred orientation of the hexagonal lattice inside the pore.

A note of caution regarding X-ray determination of LC or crystal orientation in nanopores. Considering the above orientation of the hexagonal lattice, the $\theta/2\theta$ X-ray diffraction method that has been used previously to scan the {100} intensity only along the pore axis[8,10] may, through slight misalignment, easily miss the point where one of the two smaller {100} rings just touches the Ewald sphere; a rotation of both the reciprocal space (by θ) and the detector (by 2θ) around the vertical axis in Figure 2d describes the situation during the $\theta/2\theta$ scan where a powder diffraction method is used on what is effectively a fiber sample. Missing a reflection in such a way may easily lead to erroneous conclusions about the orientation of the columns.

2. HAT6 and HAT6/TNF Complex. In order to obtain pure planar anchoring of columns of these systems, the AAO surface was modified with an alkylsilane (hexadecyltrichlorosilane, HTS). The effect of HTS functionalization of glass surface on anchoring of HAT6 can be seen in Figure S1b,c (Supporting Information).[31] We are thus able to study the configuration of HAT in confinement where planar anchoring is enforced.

For the "ordered" columnar Col_{hex} phase of HAT6, often denoted Col_{ho}, the dominant reflection groups are {100}, corresponding to an interplanar distance of $d_{(100)} = 1.83$ nm (equivalent to a center-to-center distance between adjacent columns of $a = (2/\sqrt{3})\, d_{(100)} = 2.11$ nm) and the {001} representing the intracolumnar disc-to-disc distance of 0.341 nm. Parts a, c, and e of Figure 3 show the diffraction patterns of HAT6 in HTS-modified 20, 70, and 400 nm pore diameter AAO templates at $\Phi = 80°$. They all show a hexagonal pattern highly oriented with the [100] direction perpendicular to the pore axis, as described above for the CBZ dendron. Thus, the columns of HAT6 also prefer to bend and adopt a CC configuration in the pores, rather than lying axially. Note that the additional weaker arcs, seen particularly in Figure 3e, are likely due to some columns being homeotropically, *i.e.*, radially, aligned in pores whose surface was not completely silanized.

In order to stiffen the columns of HAT6, we added to it the acceptor compound TNF, thus obtaining a charge-transfer HAT6−TNF complex. According to one proposed structural model,[17] the stiffening is due to the long axis of the TNF molecules lying parallel to the column axis. A 1:1 mixture of the two compounds

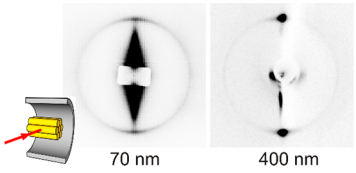

Figure 4. SAXS patterns of helicene in 70 and 400 nm AAO templates recorded at $\Phi = 80°$.

was prepared. The columnar phase of the complex was stable from below rt to 273 °C. The complex columns also show planar anchoring on the HTS-modified surface (Figure S1e, Supporting Information). Figure 3b displays the diffraction pattern of the complex in the modified 20 nm template at $\Phi = 80°$. The {100} reflections are seen to condense on the equator (perpendicular to the pore axis). This behavior means that the {100} reciprocal space rings degenerate into a single ring that lies in the equatorial plane perpendicular to the pore axis, as schematically drawn in Figure 3h. Thus, the columns adopt axial orientation (Figure 3g). Confirming this axial orientation, the intracolumnar {001} reflection shows up on the meridian in the wide-angle diffraction pattern (Figure S4, Supporting Information). The 70 nm template shows a similar diffraction pattern, except that there are four additional weak off-equator {100} spots in the SAXS region (Figure 3d). This indicates that, while most LC columns are oriented axially, a small proportion is perpendicular to the pore axis. The minority circular columns are likely to be restricted to the periphery of the pore, close to the wall, where curvature is the lowest. In the 400 nm pores, the columns switch orientation and adopt the predominantly CC configuration (Figure 3f). In agreement with the SAXS, the WAXS pattern of the 400 nm template (Figure S4) shows no (001) diffraction on the meridian. The observed gradual change of column configuration will be discussed in Section 5.

3. Helicene. The diffraction patterns of the tetradodecyloxy heterohelicene infiltrated in 70 and 400 nm pores of the AAO templates (Figure 4) show typical features of axial column orientation, with only equatorial reflections of the {100} group. The strong streak-like small-angle equatorial scatter in the 70 nm pattern is due to the AAO pores themselves, as in Figure 3a,c. The columns of the helicene are believed to be the stiffest among the compounds used in the present study, due to their intertwined 6-strand helical structure shown in Figure 1c.[19] Thus, the observed behavior of the helicene follow the general trend revealed in this study, that axial orientation of the column is promoted by their increasing bending modulus.

4. Geometry Consideration. Table 1 summarizes the configurations of the columnar phase of the different compounds in AAO pores under planar anchoring.

TABLE 1. Summary of the Configurations of Different Compounds in AAO Pores under Planar Anchoring[a]

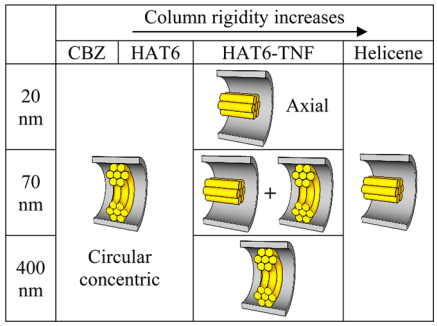

[a] The rigidity of the LC columns increases from left to right.

We observed that the orientation of the columns changes from circular concentric to axial as the rigidity of the columns increase. Additionally, when the column rigidity is borderline, increasing pore diameter can change the configuration from axial to circular. The obvious question posed by the present study is why only stiff columns show axial orientation, when such configuration minimizes the bending energy and should apparently be favorable even in compounds with lower bend constant. Our proposed explanation is that, unlike in the case of nematic or smectic LCs, with columnar LCs we also have to take into account two additional factors: (i) in the case of axial columns, the variation of anchoring energy as a function of the local inclination angle between the hexagonal lattice planes and the pore wall, and (ii) the energy of distortion of the hexagonal lattice in the *xy* plane. The anchoring energy clearly depends on whether the substrate is faced by a {100}, {110} or a noncrystallographic plane. The GISAXS results shown above confirm that the densely packed {100} plane anchoring is energetically the most favored.[32] Moving around the circular wall of a nanopore a hexagonal monodomain will be in this favorable anchoring orientation only at six positions, with an unfavorable orientation everywhere else; see Figure 5d. The situation can be improved either by distorting the hexagonal lattice or by breaking up the monodomain into smaller domains with the inevitable creation of grain boundaries. Lattice distortion is likely to involve the creation of a large number of defects such as the longitudinal edge dislocations illustrated in Figure 5f.[28]

5. Energy of Lattice Distortion. Here we make a simple estimate of the energies of the axial and circular concentric column arrangements inside the AAO nanopores. We derive energy expressions for the two modes of packing of hexagonal columns inside cylindrical pores, axial and circular, and compare their dependencies on the pore radius.

The distortion free energy of a columnar phase can be described in general as[27]

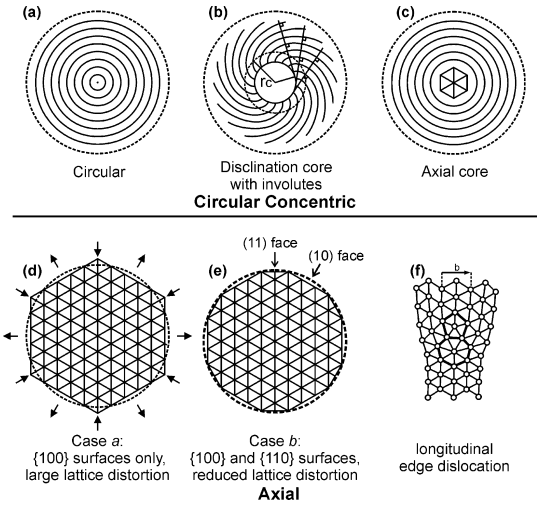

Figure 5. (a–c) Models of the core of an $S = 1$ disclination in columnar LCs (circular and spiralling lines represent the columns). (a) Concentric circles observed in small droplets.[7] The situation observed in the CBZ dendron (Figure 2g) is closely related. (b) Core region of radius r_c.[26,28] (c) Concentric circular arrangement with axial columns in the core.[28,29] (d–f) Schematic drawings of possible *axial* arrangement of columns inside AAO pores. (d) Axial with only (100) surfaces, large lattice distortion. (e) Axial with both (100) and (110) surfaces to minimize lattice distortion. (f) Model of a longitudinal edge dislocation (view down the columns); many such dislocations are required if an axial columnar domain needs deforming in order to allow a crystallographic plane to follow the curvature of the circular inner wall of an AAO wall. b = Burgers vector.

$$F = \frac{1}{2}B\left(\frac{\partial u_x}{\partial x}+\frac{\partial u_y}{\partial y}\right)^2 + \frac{1}{2}C\left[\left(\frac{\partial u_x}{\partial x}-\frac{\partial u_y}{\partial y}\right)^2 + \left(\frac{\partial u_x}{\partial y}+\frac{\partial u_y}{\partial x}\right)^2\right] + \frac{1}{2}K_3\left[\left(\frac{\partial^2 u_x}{\partial z^2}\right)^2 + \left(\frac{\partial^2 u_y}{\partial z^2}\right)^2\right] \quad (1)$$

Here **u**(**r**) is the vector field of "column displacement" of the columnar phase, with z being the uniaxial direction. The first term corresponds to the radially homogeneous compression (dilation) of the columns, the second term to pure shear, and the third to bending of the columns. Note that the splay and twist elastic constants K_1 and K_2 are subsumed in the compression and shear moduli B and C.[24] For axial arrangement, there is no bending of the columns, so the third term is zero. A further simplification of the equation, is to estimate the first two terms as a summation over all the lattice points, assuming an effective distortion Δu_i for the ith column. Hence the distortion free energy F_{axial} per unit length along pore axis can be written as

$$F_{axial} = \sum_i \frac{1}{2}B'(\Delta u_i)^2 = \frac{NB'}{2}\langle \Delta u^2 \rangle \quad (2)$$

Here, $N = (2\pi R^2)/(\sqrt{3}a^2)$ is the total number of columns inside the AAO pore (R is the radius of the pore and a is the lattice parameter of the hexagonal phase), and B' should have the same order of magnitude as B and C.

The mean square average effective distortion $<\Delta u^2>$ can be estimated from the distortion required of the lattice at the inner surface of the AAO pore. In case a (Figure 5d), where all the surface is {100}, the distortion of columns at the pore wall $<\Delta u_s^2>$ is proportional to the square of the pore radius R^2. In order to minimize the total distortion energy, this distortion should be distributed evenly over all the lattice points N, then $<\Delta u^2 \geq <\Delta u_s^2> N_s^2/N^2$, where N_s is the number of surface columns, hence proportional to R, and N is the total number of columns in the pore, hence proportional to R^2. Consequently, $<\Delta u^2>$ is independent of R, and the total distortion free energy F_{dist} is proportional to the number of columns in the pore and to R^2. Hence, F_{dist} can be expressed as

$$F_{dist} = B_a R^2 \quad (3)$$

where B_a is a constant. A surface energy term should also be included. As there are only {100} surface planes, the total free energy (per unit length along pore axis) for case (a) can be expressed as

$$F_{axial,a} = B_a R^2 + 2\pi R\sigma_{(100)} \quad (4)$$

where σ is surface free energy per unit area. From eq 4 it is clear that the distortion energy increases quite steeply with increasing pore radius. This can be reduced by allowing other surface planes such as {110} (case b, Figure 5e). However, the less closely packed {110} surfaces have a higher surface energy $\sigma_{(110)}$. In case b, the angle between the AAO wall and the ideal {100} surface anywhere along the wall's circumference can be approximated by an appropriate combination of (100) and (110) steps. This way, the distortion never needs to exceed the length a of one unit cell. The distortion $<\Delta u_s^2>$ is thus proportional to a^2 instead of R^2, and the total free energy for case b is

$$F_{axial,b} = B_b a^2 + 2\pi R\left(\frac{1}{2}\sigma_{(100)} + \frac{1}{2}\sigma_{(110)}\right) \quad (5)$$

Here, {100} and {110} surface areas were assumed to be equal.

A third way (case c) of reducing the lattice distortion while minimizing unfavorable surface free energy is to have multiple domains in the AAO pore, but in this case domain boundaries are introduced. In this case, the lattice distortion energy will again be proportional to a^2, while the size of the grain boundary should be proportional to R, so the total free energy for case (c) becomes

$$F_{axial,c} = B_c a^2 + 2\pi R\sigma_{(100)} + k_c R\sigma_g \quad (6)$$

where B_c and k_c are constants and σ_g is the free energy of the domain boundary per unit boundary area.

On the other hand, in the case of the observed circular concentric configuration of the columns in the

pores (Figure 5a), the distortion energy comes from column bending (third term in eq 1). For a circular column with a bending radius r:

$$\left(\frac{\partial^2 u_x}{\partial z^2}\right)^2 + \left(\frac{\partial^2 u_y}{\partial z^2}\right)^2 = \frac{1}{r^2} \quad (7)$$

The appropriate free energy of bending per unit length of pore is

$$F_{\text{bend}} = \pi K_3 \int_a^R \frac{1}{r^2} r dr = \pi K_3 \ln\left(\frac{R}{a}\right) \quad (8)$$

Thus, the total free energy for this case is

$$F_{\text{circ}} = \pi K_3 \ln\left(\frac{R}{a}\right) + 2\pi R\sigma_{(100)} \quad (9)$$

From the above considerations, it can be concluded that, for axial arrangement of columns, the distortion free energy is linearly proportional to R or increases with an even higher power of R when the additional R^2 term is counted in case (a). At the same time, for the circular arrangement it is proportional to ln R instead. Consequently for pores with a radius larger than a critical value R_c, CC arrangement is favored. The changeover from axial to circular is indeed seen in the case of the HAT6–TNF complex, where the critical radius R_c turns out to be about 35 nm (see above). In fact, if the critical size R_c is larger than the lattice parameter a, a mixed model may be possible with an axial or isotropic core and a circular or involute periphery (Figure 5b,c).

CONCLUSION

We demonstrated experimentally that the orientation of the columnar phase is determined by the competition between the distortion energy of the 2-d lattice in the axial orientation and the bend energy of the columns in the CC configuration. Apparently, only in the case of stiff columns does axial orientation present a viable alternative. As the current and previous examples seem to indicate, the necessary high bending modulus is achieved by complexation, formation of multistranded helices, or increasing the size of the discotic molecule. The axial orientation could be desirable for organic electronic applications.[33] The results of this study can help guide the design of hybrid LC–inorganic systems with desired column arrangements.

METHODS

Sample Preparation. The synthesis of CBZ dendron is described in refs 15 and 34, and that of HAT6 is described in ref 35. TNF was purchased from Aldrich. To prepare the HAT6–TNF complex, the two components were mixed in dichloromethane and dried. The tetrafunctionalized LC heterohelicene was synthesized as described previously.[18] AAO membranes containing 100 μm deep pores with 20, 70, and 400 nm diameter were prepared according to procedures reported elsewhere.[36] To change the polarity of the inner surface, selected AAO templates were treated with hexadecyltrichlorosilane (HTS) (Fluorochem) vapor at 90 °C for 3 h. Compounds were infiltrated into the nanopores in their isotropic liquid state under vacuum. Material remaining on the surface was carefully removed. All samples were slowly cooled from the isotropic liquid into the columnar phase at 0.1 °C/min before further investigations.

2-d X-ray Diffraction. The X-ray diffraction was performed with an in-house X-ray facility. X-rays were produced using a Rigaku MicroMax 007 microfocus copper rotating anode generator running at 40 kV, 20 mA and focused onto the crystal using confocal multilayer optics. The temperature was controlled by an Oxford Cryosystems Cryostream 700 jet. Data were accumulated using a MarResearch MAR345 image plate detector system.

Microscopy Observation. Tapping mode AFM imaging was performed at rt on a Bruker Multimode 8 instrument with Nanoscope V controller. An Olympus BX-50 transmitted-light polarizing microscope equipped with a Mettler FP82 hotstage and a Coolsnap-Pro digital camera was used to observe the texture of the LCs.

GISAXS. Samples for GISAX were prepared by casting thin films on substrate surface *via* solution. The obtained thin films were heated to isotropic liquid in vacuum oven and then slowly cooled into the liquid crystal phase. GISAXS measurements were carried out at Station I16 at Diamond Light Source (U.K.).

Conflict of Interest: The authors declare no competing financial interest.

Acknowledgment. We are greatly indebted to Professor Thomas Katz of Columbia University for kindly donating the helicene sample. We thank Dr. Nicholas Mullin for helpful advice on AFM. For help with X-ray synchrotron experiments we thank Drs. G. Nisbet and Prof. S. Collins of I16 at Diamond Light Source. Financial support is acknowledged from the joint NSF-EPSRC PIRE project "RENEW" (EPSRC Grant No. EP_K034308), the Leverhulme Foundation ((RPG-2012-804) and, for G.U., the "1000 Talents" program of the Government of China. Financial support for V.P. by the NSF (DMR-1066116, DMR-1120901, and OISE-1243313) and the P. Roy Vagelos Chair at Penn is acknowledged.

Supporting Information Available: Polarized optical micrographs, SAXS patterns of compounds in AAO membranes at different incidence angles and with pores of different diameters, and wide-angle scattering patterns of LC-loaded membranes with pores of different diameters. This material is available free of charge *via* the Internet at http://pubs.acs.org.

REFERENCES AND NOTES

1. Kruglova,O. V.; *Discotic Liquid Crystals: From Dynamics to Conductivity*; IOS Press: Amsterdam, 2007.
2. Kumar, S. Functional Discotic Liquid Crystals. *Isr. J. Chem.* **2012**, *52*, 820–829.
3. Kato, T.; Yasuda, T.; Kamikawa, Y.; Yoshio, M. Self-assembly of functional columnar liquid crystals. *Chem.Commun.* **2009**, 729–739.
4. Pisula, W.; Feng, X.; Müllen, K. Tuning the Columnar Organization of Discotic Polycyclic Aromatic Hydrocarbons. *Adv. Mater.* **2010**, *22*, 3634–3649.
5. Wang, C. C.; Lu, H. C.; Liu, C. C.; Jenq, F. L.; Wang, Y. H.; Houng, M. P. Improved Extraction Efficiency of Light-Emitting Diodes by Modifying Surface Roughness with Anodic Aluminum Oxide Film. *IEEE Photon. Technol. Lett.* **2008**, *20*, 428–430.
6. Cerclier, C. V.; Ndao, M.; Busselez, R.; Lefort, R.; Grelet, E.; Huber, P.; Kityk, A. V.; Noirez, L.; Schönhals, A.; Morineau, D.

Structure and Phase Behavior of a Discotic Columnar Liquid Crystal Confined in Nanochannels. *J. Phys. Chem. C* **2012**, *116*, 18990–18998.
7. Zhang, R. B.; Zeng, X. B.; Prehm, M.; Liu, F.; Grimm, S.; Geuss, M.; Steinhart, M.; Tschierske, C.; Ungar, G. Honeycombs in Honeycombs: Complex Liquid Crystal Alumina Composite Mesostructures. *ACS Nano* **2014**, *8*, 4500–4509.
8. Steinhart, M.; Zimmermann, S.; Göring, P.; Schaper, A. K.; Gösele, U.; Weder, C.; Wendorff, J. H. Liquid Crystalline Nanowires in Porous alumina: Geometric Confinement Versus Influence of Pore Walls. *Nano Lett.* **2005**, *5*, 429–434.
9. Kityk, A. V.; Busch, M.; Rau, D.; Calus, S.; Cerclier, C. V.; Lefort, R.; Morineau, D.; Grelet, E.; Krause, C.; Schönhals, A.; et al. Thermotropic Orientational Order of Discotic Liquid Crystals in Nanochannels: An Optical Polarimetry Study and a Landau-de Gennes Analysis. *Soft Matter* **2014**, *10*, 4522–4534.
10. Duran, H.; Azanza, B. H.; Steinhart, M.; Gehrig, D.; Laquai, F.; Feng, X.; Müllen, K.; Butt, H.; Floudas, G. Arrays of Aligned Supramolecular Wires by Macroscopic Orientation of Columnar Discotic Mesophases. *ACS Nano* **2012**, *6*, 9359–9365.
11. Pisula, W.; Kastler, M.; Wasserfallen, D.; J. Davies, R. J.; García-Gutiérrez, M. C.; Müllen, K. From Macro- to Nanoscopic Templating with Nanographenes. *J. Am. Chem. Soc.* **2006**, *128*, 14424–14425.
12. Caprion, D. Discotic Molecules in Cylindrical Nanopores: A Monte Carlo Study. *Eur. Phys. J. E* **2009**, *28*, 305–313.
13. Crawford, G. P.; Vilfan, M.; Doane, J. W. Escaped-radial Nematic Configuration in Submicrometer-size Cylindrical Cavities: Deuterium Nuclear-magnetic-resonance Study. *Phys. Rev. A* **1991**, *43*, 835–842.
14. Ondris-Crawford, R. J.; Crawford, G. P.; Zumer, S.; Doane, J. W. Curvature-induced configuration transition in confined nematic liquid crystals. *Phys. Rev. Lett.* **1993**, *70*, 194–197.
15. Percec, V.; Glodde, M.; Bera, T. K.; Miura, Y.; Shiyanovskaya, I.; Singer, K. D.; Balagurusamy, V. S. K.; Heiney, P. A.; Schnell, I.; Rapp, A.; et al. Self-organization of Supramolecular Helical Dendrimers Into Complex Electronic Materials. *Nature* **2002**, *419*, 384–387.
16. Tsukruk, V. V.; Wendorff, J. H.; Karthaus, O.; Ringsdorf, H. Packing of Columns in Langmuir-Blodgett Films of Discotic Mixtures with Charge-Transfer Interactions. *Langmuir* **1993**, *9*, 614–618.
17. Kruglova, O.; Mendes, E.; Yildirim, Z.; Wübbenhorst, M.; Mulder, F. M.; Stride, J. A.; Picken, S. J.; Kearley, G. J. Structure and Dynamics of a Discotic Liquid-Crystalline Charge-Transfer Complex. *ChemPhysChem* **2007**, *8*, 1338–1344.
18. Phillips, K. E. S.; Katz, T. J.; Jockusch, S.; Lovinger, A. J.; Turro, N. J. Synthesis and Properties of an Aggregating Heterocyclic Helicene. *J. Am. Chem. Soc.* **2001**, *123*, 11899–11907.
19. Shcherbina, M. A.; Zeng, X. B.; Tadjiev, T.; Ungar, G.; Eichhorn, S. H.; Philips, K. E. S.; Katz, T. J. Hollow Six-stranded Helical Columns of a Helicene. *Angew. Chem. Int. Ed* **2009**, *48*, 7837–7840.
20. Sharma, D.; Rey, A. D. Simulation of Texture Formation Processes in Carbonaceous Mesophase Fibres. *Liq. Cryst.* **2003**, *30*, 377–389.
21. Jian, K. J.; Shim, H. S.; Schwartzman, A.; Crawford, G. P.; Hurt, R. H. Orthogonal Carbon Nanofibers by Template-Mediated Assembly of Discotic Mesophase Pitch. *Adv. Mater.* **2003**, *15*, 164–167.
22. Kundu, S.; Ogale, A. A. Rheostructural Studies of a Discotic Mesophase Pitch at Processing Flow Conditions. *Rheol. Acta* **2010**, *49*, 845–854.
23. Yan, J.; Rey, A. D. Texture Formation in Carbonaceous Mesophase Fibers. *Phys. Rev. E* **2002**, *65*, 031713.
24. Selinger, J. V.; Bruinsma, R. F. Hexagonal and nematic phases of chains. I. Correlation functions. *Phys. Rev. A* **1991**, *43*, 2910–2921.
25. Bouligand, Y. Defects and Textures of Hexagonal Discotics. *J. Phys. (Paris)* **1980**, *41*, 1307–1315.
26. Kleman, M. Developable Domains in Hexagonal Liquid Crystals. *J. Phys. (Paris)* **1980**, *41*, 737–745.
27. Oswald, P.; Pieranski, P. *Smectic and Columnar Liquid Crystals*; Taylor & Francis: Boca Raton, FL, 2006.
28. Bouligand, Y. Geometry of (non smectic) hexagonal mesophases. *J. Phys. (Paris)* **1980**, *41*, 1297–1306.
29. Sallen, L.; Oswald, P.; Geminard, J. C.; Malthete, J. Surface Tension and Elasticity of Hexagonal Columnar Mesophases. *J. Phys. II* **1995**, *5*, 937–961.
30. As is well-known, the untreated silicon surface is actually covered by an oxide layer; hence, the LC anchoring on that surface and on the alumina surface are expected to be the same, as shown previously in ref 7.
31. With respect to silane treatment, in our experience,[7] the alumina surface acts very similarly to the natural oxide layer on the surface of Si.
32. Bramble, J. P.; Tate, D. J.; Revill, D. J.; Sheikh, K. H.; Henderson, J. R.; Bushby, R. J.; Evans, S. D.; Liu, F.; Zeng, X. B.; Ungar, G. Planar Alignment of Columnar Discotic Liquid Crystals by Isotropic Phase Dewetting on Chemically Patterned Surfaces. *Adv. Funct. Mater.* **2010**, *20*, 914–920.
33. Haverkate, L. A.; Zbiri, M.; Johnson, M. R.; Carter, E.; Kotlewiski, A.; Picken, S.; Mulder, F. M.; Kearley, G. J. Electronic and Vibronic Properties of A Discotic Liquid-Crystal and Its Charge Transfer Complex. *J. Chem. Phys.* **2014**, *140*, 014903−1–014903−8.
34. Percec, V.; Glodde, M.; Peterca, M.; Rapp, A.; Schnell, I.; Spiess, H. W.; Bera, T. K.; Miura, Y.; Balagurusamy, V. S. K.; Aqad, E.; et al. Self-Assembly of Semifluorinated Dendrons Attached to Electron-Donor Groups Mediates Their π-Stacking via a Helical Pyramidal Column. *Chem.—Eur. J.* **2006**, *12*, 6298–6314.
35. Boden, N.; Borner, R. C.; Bushby, R. J.; Cammidge, A. N.; Jesudason, M. V. The synthesis of triphenylene-based discotic mesogens New and improved routes. *Liq. Cryst.* **1993**, *15*, 851–858.
36. Masuda, H.; Fukuda, K. Ordered Metal Nanohole Arrays Made by a Two-Step Replication of Honeycomb Structures of Anodic Alumina. *Science* **1995**, *268*, 1466–1468.